Check for updates

High-quality factor mid-infrared absorber based on all-dielectric metasurfaces

Fuming Yang,[1,2] Zhongzhu Liang,[1,2,3,4] Dejia Meng,[1,*] (iD)
Xiaoyan Shi,[1,2,3] Zheng Qin,[1,2] (iD) Rui Dai,[3] Chunfang Sun,[3]
Yingzheng Ren,[1,2] Jiajing Feng,[1,2] and Wenjun Liu[1,2]

[1] *State Key Laboratory of Applied Optics, Changchun Institute of Optics, Fine Mechanics and Physics, Chinese Academy of Sciences, Changchun, Jilin, 130033, China*
[2] *University of the Chinese Academy of Sciences, China*
[3] *Center for Advanced Optoelectronic Functional Materials Research and Key Laboratory of UV Light-Emitting Materials and Technology of Ministry of Education, College of Physics, Northeast Normal University, Changchun 130024, China*
[4] *liangzz@nenu.edu.cn*
*djmeng@sklao.ac.cn

Abstract: The absorption spectrum of metasurface absorbers can be manipulated by changing structures. However, narrowband performance absorbers with high quality factors (Q-factor) are hard to achieve, mainly for the ohmic loss of metal resonators. Here, we propose an all-dielectric metasurface absorber with narrow absorption linewidth in the mid-infrared range. Magnetic quadrupole resonance is excited in the stacked Ge-Si_3N_4 nanoarrays with an absorption of 89.6% and a Q-factor of 6120 at 6.612 μm. The separate lossless Ge resonator and lossy Si_3N_4 layer realize high electromagnetic field gain and absorption, respectively. And the proposed method successfully reduced the intrinsic loss of the absorber, which reduced the absorption beyond the resonant wavelength and improved the absorption efficiency of Si_3N_4 in the low loss range. Furthermore, the absorption intensity and wavelength can be modulated by adjusting the geometric parameters of the structure. We believe this research has good application prospects in mid-infrared lasers, thermal emitters, gas feature sensing, and spectral detection.

1. Introduction

Metasurfaces or metamaterials absorbers (MAs) with high performance and specific functions can construct nearly perfect absorption in subwavelength thickness [1–3]. The MAs based on the classic Metal-Dielectric-Metal (MDM) sandwich structure have been widely studied from visible light to microwave ranges [4–7]. These studies have promising applications in solar energy capture [8,9], radiative cooling [10,11], detection [12–14], camouflage [15,16], etc. High spectral selectivity and resolution have a strong demand for narrowband response. The narrowband MAs can absorb specific wavelengths of radiation with solid spectral selectivity in the fields of spectral sensing [17,18] and thermal emitters [19–21]. However, the absorption bandwidth of metallic MAs is limited due to the apparent intrinsic loss caused by ohmic damping [22]. Some resonance modes with low dissipation rates can suppress the intrinsic loss to improve the absorption quality factor (Q-factor) of metallic MAs, such as guided-mode resonance [23], lattice resonance [24,25], and high-order mode gain medium [26]. However, the absorption caused by ohmic loss is accompanied by a thermal effect instead of photogenerated carriers, which limits their application in optoelectronic devices.

In recent years, all-dielectric metasurfaces based on Mie resonances have attracted much attention due to their low-loss characteristic and provide rich optical resonance properties [27–30], which have critical applications in wavefront control such as metalens [31,32] and holography [33,34]. Lossless dielectric resonators in the metasurface could exhibit magnetic and electric

dipoles and higher-order resonances, which is an effective method for narrowband response [35]. As for a lossy system, lossy materials need to be introduced into dielectric resonators to achieve absorption. But there is a 50% absorption limit in a single resonance mode for dielectric films with subwavelength thicknesses, and the same goes for MAs [36,37]. The coupling effect of antisymmetric electromagnetic modes can break the limitation and 100% absorption achieved by introducing appropriate intrinsic losses to match the radiation losses [38–41]. All-dielectric MAs based on Si and Ge resonators have been realized in the near-infrared and visible light bands [42,43]. The absorption originates from the resonance response provided by the high refractive index lossy dielectric unit. However, achieving narrowband and high absorption in all-dielectric MAs simultaneously in the mid-infrared range (3-14 μm) is still challenging. Some reports of mid-infrared high-Q absorbers based on metallic metasurface [44]. For example, the Q-factor of the absorbers based on cross or ring gold resonators reaches 30 and 118, respectively [22,45]. And a method of constructing high-Q dielectric resonators using a high-reflectivity metal layer could increase the Q-factor to more than 1000 by increasing the absorption of metal [46,47]. For all-dielectric MAs, the index of the commonly used infrared lossy materials such as Si_3N_4 and SiO_2 are too low to realize the corresponding resonant mode response requires a larger size/wavelength ratio, which means an increase in intrinsic absorption effect, which would cause the expansion of absorption bandwidth.

In this study, we proposed a high-Q absorber based on an all-dielectric metasurface in the mid-infrared range. The narrowband absorption is based on the separation of resonance and lossy area. First, a lossless $Ge\text{-}CaF_2$ resonator was designed to generate high-Q resonance. The magnetic quadrupole mode and magnetic dipole mode with ultra-narrow linewidth are generated at P_1 (6.612 μm) and P_2 (8.236 μm), respectively. Then, a selective narrowband absorber is achieved by applying the high-Q resonance to the lossy Si_3N_4 layer. The separate lossless Ge resonator and lossy layer realize high electromagnetic field gain and high absorption, respectively, while reducing the intrinsic loss of the material. Furthermore, due to the size sensitivity of resonances, the absorption intensity and wavelength can be modulated by adjusting the geometric parameters of the structure. Therefore, the high-Q wavelength-tunable absorption capability makes this research promising for applications in miniature infrared spectrometers, mid-infrared lasers, infrared detection and sensing.

2.   Structure and design

The schematic diagram of the all-dielectric high-Q absorber proposed in this paper is shown in Fig. 1, where Si_3N_4 nanoarray and Ge nanoarray on a CaF_2 substrate in sequence, with a unit period P of 3.38 μm. The thicknesses of the Si_3N_4 and Ge nanopillars are $H_0 = 100$ nm and
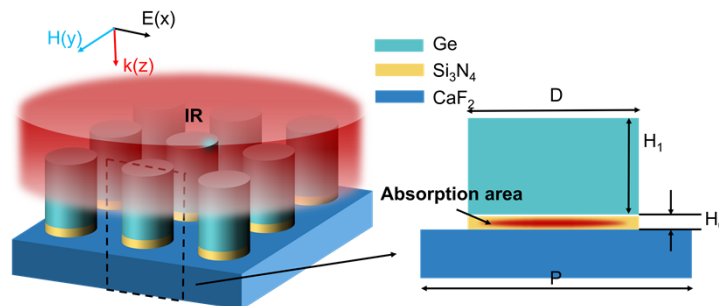

Fig. 1. Schematic diagram of the all-dielectric narrowband absorber. P represents the period of the unit cell, and H_0 and H_1 represent the heights of the Si_3N_4 and Ge layers, respectively. The common diameter of the nanopillars is D.

$H_1 = 4.38\,\mu m$, respectively, and their common diameter D is $2\,\mu m$. The loss of CaF_2 and Ge can be ignored in the research wavelength range, and the refractive index of the two materials are fixed at 1.4 and 4 in the simulation. We simulated the performance of the structure by using the finite-difference time-domain (FDTD) method. The boundary conditions in the X and Y directions are periodic, and the normal incident infrared light reaches the structure along the Z-axis. The structure is polarization-independent, so we use linearly polarized light with the electric field direction along the X-direction for simulations, whose wave vectors and field directions are shown in Fig. 1.

3. Result and discussion

Figure 2 shows the reflection (R), transmission (T), and absorption (A) spectrums of the Ge-Si_3N_4-CaF_2 lossy absorber and the Ge-CaF_2 lossless resonator, respectively. The absorption can be expressed as A = 1 - R - T. Under the excitation of normal incident electromagnetic waves, the subwavelength nanoarrays based on high-refractive-index dielectric material can excite different orders of electrical and magnetic resonances due to the Mie resonance effect, which shows abnormal reflection or transmission spectrum. Based on this, we constructed a lossless resonator structure using Ge-CaF_2 units, in which the substrate is CaF_2, and the Ge nanoarrays are the resonators. The scattering properties are shown in Fig. 2(c). Two ultra-narrow resonance peaks are generated at P_1 ($6.612\,\mu m$) and P_2 ($8.236\,\mu m$). Compared with the adjacent wavelength, the reflectivity of P_1 decreased while P_2 increased significantly. Before introducing lossy materials, the structure had no absorption in the entire spectral band, and the absorptivity was zero, as shown in Fig. 2(d). Then, we inserted a 100 nm-thick Si_3N_4 thin disk with the same diameter under the Ge resonator, as shown in Fig. 2(a). The Si_3N_4 disk will not excite new resonant modes to affect the Ge resonator for the mismatch between size and wavelength. Only Transmission and reflection at P_1 and P_2 are suppressed significantly, and the overall scattering curves are consistent with the case without lossy material. Indeed, we obtained two absorption peaks with high Q-factor, P_1 and P_2, corresponding to the original resonance peak, as shown in Fig. 2(b). Among the Ge-Si_3N_4-CaF_2 absorber, the absorptivity of P_1 is 89.6%, the FWHM of the absorption peak is 1.08 nm, and the Q-factor is 6120. The absorptivity of P_2 is 38.9%, the FWHM is 22.2 nm, and the Q factor is 371. The Q-factor is given by $Q = \lambda / FWHM$, where λ is the absorption peak wavelength, and FWHM is the absorption peak full width at half maximum.

The intense resonance modes at the high-Q resonance peaks P_1 and P_2 enhance the absorption effect of the lossy material Si_3N_4, thus achieving high-Q absorption. Figure 3(a) lists the refractive index dispersion curves of Si_3N_4 at wavelengths from 2 to $14\,\mu m$ [48]. The imaginary part of the refractive index k means extinction coefficient. The region with a large extinction coefficient is concentrated in the band of 10-14 μm, while the region with a shorter wavelength is smaller, which means weaker absorbing ability. We compared the absorption property of insert Si_3N_4 in different situations, as shown in Fig. 3(b). All films were placed on a CaF_2 substrate. The yellow dotted curve in Fig. 3(b) shows the absorption of the 100 nm thick Si_3N_4 film in the wavelength range of 6-14 μm, which is consistent with the distribution of the extinction coefficient. At P_3 ($\lambda = 12\,\mu m$), the maximum absorptivity reaches 24.6%, which is only 2.6% at $6\,\mu m$. As shown by the green curve in Fig. 3(b), we reduced the filling ratio of lossy material by patterning the Si_3N_4 layer, which leads to a decrease in the equivalent extinction coefficient. For the convenience of nanofabrication, the radius of the Si_3N_4 disk is kept the same as that of the Ge nanopillar. Patterned Si_3N_4 restrained the intrinsic absorption of the structure, which leads the absorption at P_3 from 24.6% to 6.9%. In this process, the filling ratio of Si_3N_4 is 27.5%, and the absorptivity is 28.0% of the previous situation, which shows that the absorptivity depends on the intrinsic absorption efficiency of the material without resonance interference. At this time, due to the mismatch between the Si_3N_4 layer size and the resonant wavelength, it is difficult to excite the resonant absorption mode with high quality factor, and the thickness of the structure needs to
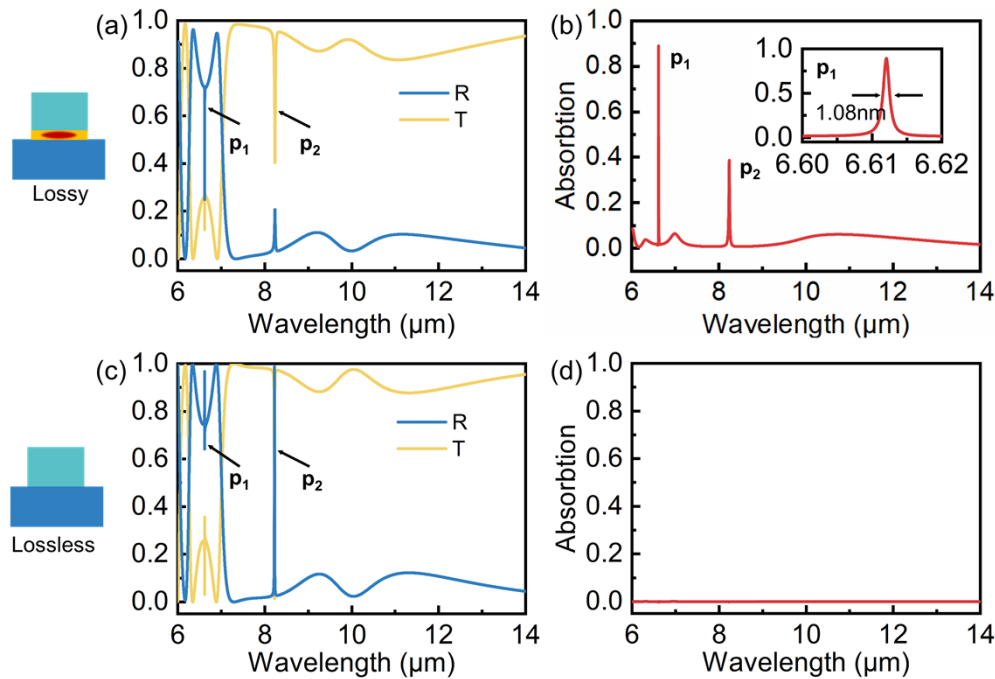
Fig. 2. (a) and (c) are the mid-infrared scattering curves of the Ge-Si$_3$N$_4$-CaF$_2$ lossy absorber and the Ge-CaF$_2$ low-loss resonator, respectively, where the transmittance is T, and the reflectance is R. (b) and (d) are the mid-infrared absorption curves of the absorber and resonator, respectively. The insert Fig. in (b) is a partial amplification of P$_1$. The FWHM of the absorption peaks P$_1$ and P$_2$ are 1.08 nm and 22.2 nm, respectively.

be increased to allow more resonant modes to exist. But the consequence is that the overall loss of the structure will rise. Therefore, we designed a low-loss Ge resonator structure to enhance the absorption of Si$_3$N$_4$ at a specific wavelength. By inserting the Si$_3$N$_4$ layer into the Ge-CaF$_2$ resonator, shown by the blue curve in Fig. 3(b), sharp absorption peaks P$_1$ and P$_2$ are generated at the two strong resonances. And the absorption of other regions is close to those without the Ge resonator. The absorption spectrum obtained by the finally adopted Ge-Si$_3$N$_4$ nanopillar array structure is shown in the red curve in Fig. 3(b), the same as in Fig. 2(b). Compared with the case of Ge-Si$_3$N$_4$ film, the absorption of P$_1$ and P$_2$ is slightly increased. In order to maintain the unity of the variables in the comparison, we maintained the parameter consistency of the Ge resonator in the Ge-Si$_3$N$_4$ nanodisk structure and the Ge-Si$_3$N$_4$ film structure. Since the final Si$_3$N$_4$ nanodisk structure is used, the parameter selection of the Ge resonator is based on the nanodisk and adapted to obtain the best absorption effect and reduce the intrinsic absorption of P$_3$, which improves the absorptivity contrast at the resonance absorption peak. The absorptivity of peaks P$_1$ and P$_2$ are not particularly dependent on the extinction coefficient of the material. Compared with the 100 nm Si$_3$N$_4$ film on the CaF$_2$ substrate, the absorption at P$_1$ and P$_2$ increased by 30 times and 8 times, respectively, while the extinction coefficient of Si$_3$N$_4$ is 0.09. This method effectively improves the absorption of Si$_3$N$_4$ in the low-loss range, which can be generalized to other low-loss materials to improve their absorptivity.

In order to explain the absorption mechanism of the design structure, electromagnetic field distribution at P$_1$ and P$_2$ were extracted, as shown in Fig. 4. The direction of the arrow represents the direction of the electric/magnetic vector field. On the whole, the intensity of the electromagnetic field in the absorber has different degrees of multiplication at the two absorption
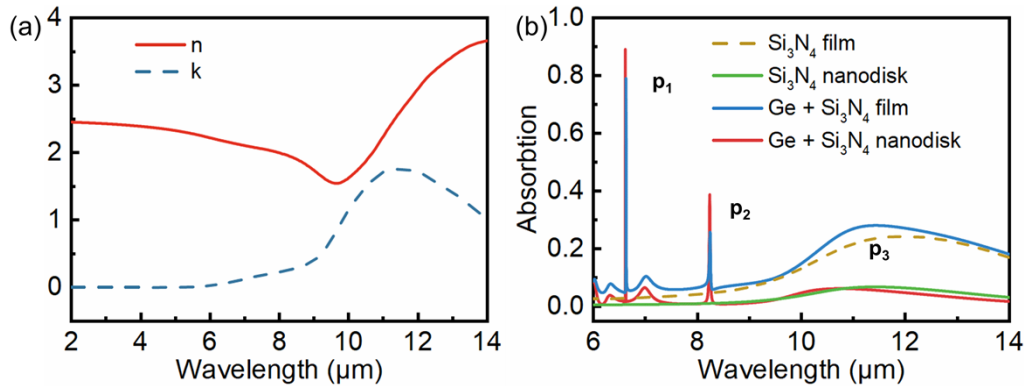
Fig. 3. (a) Refractive index actual part n, imaginary part k of Si_3N_4. (b) The absorption curves of Si_3N_4 film, Si_3N_4 nanodisk array, and the absorption after adding Ge resonator. The Si_3N_4 thickness H_0 is kept at 100 nm.

peaks, which is a significant electromagnetic field enhancement effect brought by the high-Q resonance. For the P_1 peak shown in Fig. 4(a), the electric field is concentrated in the center of the Ge column. The electric vector direction is perpendicular to the wave vector direction in the Z direction. As shown in Fig. 4(c), two opposite annular electric vectors are distributed on the XY plane. The magnetic dipole moments cancel each other and excite a magnetic quadrupole moment in Fig. 4(b). Therefore, this indicates that P_1 is dominated by magnetic quadrupole (MQ) mode. For the P_2 peak, as shown in Fig. 4(d)-(f), the electric field forms two circular vectors with the same rotation direction in the XZ plane, which excites two co-directional magnetic vectors in the YZ plane, indicating that the dominant mode is the second-order magnetic dipole (MD) mode. According to $P_{abs} = 0.5\omega\kappa|E|^2$, where ω is the angular frequency, κ is the extinction coefficient of the material, E is the electric field intensity [49], the absorptivity of the material is proportional to its extinction coefficient, and the square of the modulus of the electric field intensity in the material. The electric field at the center of the Ge resonator at P_1 has a 50-fold gain compared to the incident light, which enhances the absorption of the Si_3N_4 layer.

The response of the absorber depends mainly on the height of the Ge resonator. Each mode's resonant intensity and wavelength change accordingly when the height changes. Figure 5 shows the corresponding relationship between the changing trend of the reflection and absorption curves of the absorber wavelength and the resonator height H. The three white dotted lines in the reflection spectrum shown in Fig. 5(a) represent the electric dipole mode (ED), MQ, and MD2 modes, respectively, where P_1 corresponds to the MQ mode. The final result of the influence of different resonance modes is the change of radiation states. In Fig. 5(a), the ED and MD2 modes correspond to the radiation states of high reflectivity, while the MQ mode is the radiation state of low reflectivity. Corresponding to the absorption peak P_1, it can maintain the high-Q characteristics as a higher-order mode. According to the coupled-mode theory, the absorptivity A under the action of two coupled modes can be expressed as Eq. (1) [38]:

$$A = \frac{2\gamma_1\delta_1}{(\omega - \omega_1)^2 + (\gamma_1 + \delta_1)^2} + \frac{2\gamma_2\delta_2}{(\omega - \omega_2)^2 + (\gamma_2 + \delta_2)^2} \quad (1)$$

where ω, ω_1, and ω_2 are the angular frequency of the electromagnetic wave and the resonance angular frequency of two modes, and γ and δ are the mode's radiation loss and intrinsic loss. When only one mode is active, at the resonance frequency $\omega = \omega_1$, there is $A_{max} = 0.5$ only if $\gamma_1 = \delta_1$. Therefore, the absorption rate of the peak P_2 has an upper limit of 50%, which is only affected by a single magnetic dipole mode MD1. For P_1, it is coupled with multiple modes,
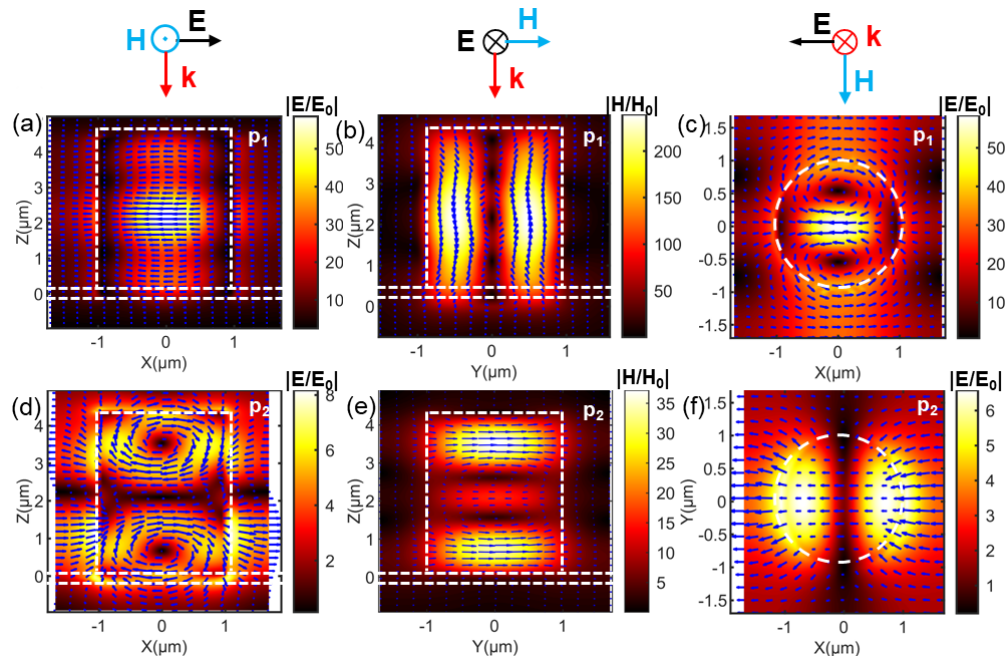
Fig. 4. The local electromagnetic field distribution of absorption peaks P_1 and P_2. (a) and (d) are the electric field distributions on the XZ plane (Y = 0) of P_1 and P_2. (b) and (e) are the magnetic field distributions on the YZ plane (X = 0) of P_1 and P_2. (c)(g) are electric field distribution on the XY plane of P_1 (Z = 2.19 μm) and P_2 (Z = 3.4 μm). The position of the XY plane depends on the center position of the P_1 and P_2 fields.

such as ED, MD2, and MQ so that A_{max} can reach 100%. As shown in Fig. 5(b), there is an apparent light-dark change process in its absorptivity. According to different characteristics, we divide the curve of P_1 with H into four regions. In region 1, the resonance coupling intensity is weak, which limits the absorption improvement. Under the multi-mode coupling in the encircled region, where in region 2, it has the characteristics of a narrow spectrum and high absorption, and the absorption rate can reach 90%. In region 3, with the increase of H, the MQ mode is suppressed by ED mode, which characteristics are entirely obscured by the ED mode, showing high reflection and low absorption. Features, in region 4, where the MQ mode that actives alone realize high-Q absorption while the maximum absorption rate is less than 50%. The absorptivity can be modulated by controlling the height or aspect ratio of the resonator.

To realize the control of absorption wavelength and intensity, we simulated the situations of different periods and Si_3N_4 thicknesses. The obtained absorption curves are shown in Fig. 6. It can be seen from Fig. 6(a) that when the period changes, both P_1 and P_2 have a slight red-shift with the increase of the period, accompanied by the change of absorption intensity. The Q-factor of P_2 shows a process of decreasing first and then increasing. The absorption is not the highest when the Q-factor is the largest, which indicates that a high Q-factor and high absorption are not completely equivalent. When the thickness of the loss material Si_3N_4 increases, as shown in Fig. 6(b), the absorption is enhanced except for the two resonance absorption peaks. The absorption wavelengths at P_1 and P_2 are almost unchanged because the absorption wavelength is determined by the relevant parameters of the upper Ge resonator. The absorption intensity of P_1 decreases with the increase of Si_3N_4 thickness because the change of loss material thickness destroys the matching condition of resonance.
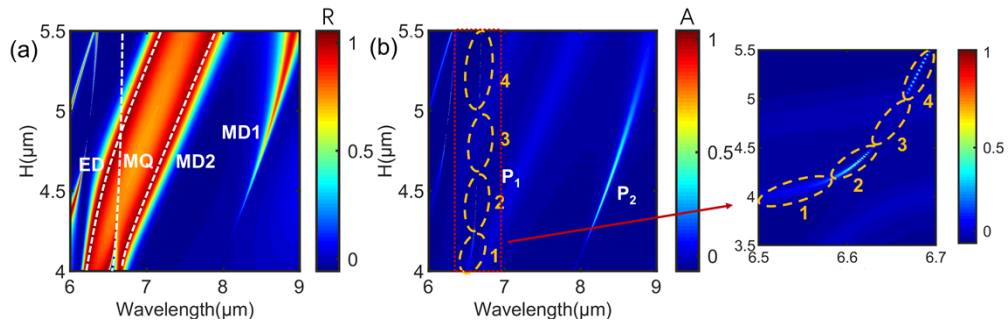
Fig. 5. Reflection (a) and absorption (b) curves of absorber at different Ge resonator heights. According to different characteristics, the curve of P_1 with H was divided into four regions, which are represented in orange dashed ellipses.
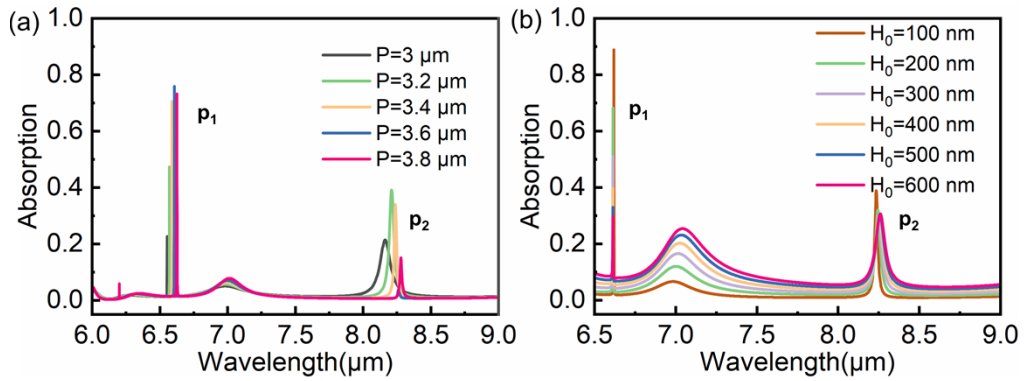

Fig. 6. The absorption curves of the absorber for the different (a) period (fill factor) P; (b) Si_3N_4 thickness H_0.
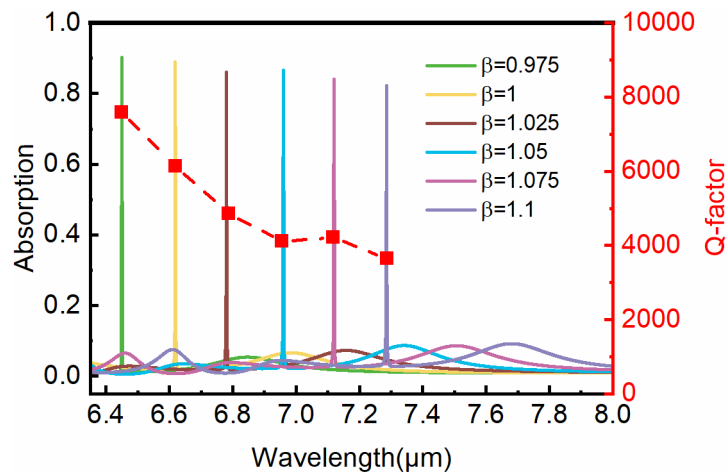

Fig. 7. Absorption curves and Q-factors corresponding to different resonator sizes. β is defined as a scaling factor to describe scaling size.

The absorption wavelength is positively related to the size of the Ge resonator. The absorption wavelength can be adjusted by proportional scaling to maintain the corresponding resonance intensity. β is defined as a scaling factor to describe scaling size. Taking the 1 μm-radius Ge column as the benchmark and maintaining the aspect ratio of the resonator, we show six absorption lines separated by a 2.5% difference of β, as shown in Fig. 7. The resonance wavelength red-shifts with the increase of the resonator size. In the 6.4-7.3 μm covered by the absorption line in Fig. 6, the absorber maintains a high absorptivity of more than 80%. And the FWHM of the absorption peak is maintained between 1-2 nm. The Q factor is maintained above 4000, where the absorption at other wavelengths in the observation range remains low, showing good contrast differences. The wavelength-modulated narrow-spectrum absorption characteristics of nm-scale linewidth and the high absorptivity contrast inside and outside the absorption peak endow the designed metasurface structure with good potential for spectral detection.

4. Conclusion

In conclusion, we propose a high-Q absorber based on an all-dielectric metasurface in mid-infrared. Unlike other all-dielectric absorbers, Resonator and absorption layer is separated in the Ge-Si_3N_4-CaF_2 absorber. The high-Q magnetic quadrupole resonance mode excited by the lossless Ge resonator enhances the absorption of the lossy Si_3N_4 thin layer so that the high absorption region occurs in a very narrow spectral width. The intrinsic loss of the absorber can be controlled by patterning Si_3N_4 to improve the wavelength contrast of absorption, which is crucial for spectral detection. The proposed absorber achieved a narrow absorption linewidth, and the obtained absorption peak P_1 has an FWHM of 1.08 nm with a Q-factor of 6120. By discussing the local electromagnetic field distribution and the Cartesian multilevel decomposition of the absorber, it is clear that the main resonant modes of absorption peaks P_1 and P_2 in the structure are magnetic quadrupole resonance and magnetic dipole resonance, respectively. The enhancement effect of the electromagnetic field accompanied by the high-Q resonance is the reason for the absorption enhancement. The absorptivity at P_1 is increased from 2.6% to 89.6%, while the extinction coefficient of Si_3N_4 is 0.09. This method effectively improves the absorption of Si_3N_4 in the low-loss range. In this way, the absorption area and wavelength are strictly limited, which can effectively improve the absorption intensity of specified electromagnetic waves in the specified material and the energy density inside the material after exposure to light. This research can also be extended to other infrared loss materials to enhance the light-matter interaction and absorption capabilities at specific needs and to improve detection sensitivity and response. Therefore, this research has good application prospects in mid-infrared laser, sensing, and photoelectric detection.

Disclosures. The authors declare no conflicts of interest.

Data availability. Data underlying the results presented in this paper are not publicly available at this time but may be obtained from the authors upon reasonable request.

References

1. N. I. Landy, S. Sajuyigbe, J. J. Mock, D. R. Smith, and W. J. Padilla, "Perfect Metamaterial Absorber," Phys. Rev. Lett. **100**(20), 207402 (2008).
2. Y. Zhou, Z. Qin, Z. Liang, D. Meng, H. Xu, D. R. Smith, and Y. Liu, "Ultra-broadband metamaterial absorbers from long to very long infrared regime," Light: Sci. Appl. **10**(1), 138 (2021).
3. J. Luo, H. Chu, R. Peng, M. Wang, J. Li, and Y. Lai, "Ultra-broadband reflectionless Brewster absorber protected by reciprocity," Light: Sci. Appl. **10**(1), 89 (2021).
4. I. Kim, S. So, A. S. Rana, M. Q. Mehmood, and J. Rho, "Thermally robust ring-shaped chromium perfect absorber of visible light," Nanophotonics **7**(11), 1827–1833 (2018).

5. Z. Li, L. Stan, D. A. Czaplewski, X. Yang, and J. Gao, "Wavelength-selective mid-infrared metamaterial absorbers with multiple tungsten cross resonators," Opt. Express **26**(5), 5616–5631 (2018).
6. C. Chen, M. Chai, M. Jin, and T. He, "Terahertz Metamaterial Absorbers," Adv. Mater. Technol. (Weinheim, Ger.) **7**(5), 2101171 (2022).
7. Y. Cheng, Y. Zou, H. Luo, F. Chen, and X. Mao, "Compact Ultra-Thin Seven-Band Microwave Metamaterial Absorber Based on a Single Resonator Structure," J. Electron. Mater. **48**(6), 3939–3946 (2019).
8. Z. Yi, J. Li, J. Lin, F. Qin, X. Chen, W. Yao, Z. Liu, S. Cheng, P. Wu, and H. Li, "Broadband polarization-insensitive and wide-angle solar energy absorber based on tungsten ring-disc array," Nanoscale **12**(45), 23077–23083 (2020).
9. J. Wu, Y. Sun, B. Wu, C. Sun, and X. Wu, "Broadband and wide-angle solar absorber for the visible and near-infrared frequencies," Sol. Energy **238**, 78–83 (2022).
10. K. Sun, C. A. Riedel, Y. Wang, A. Urbani, M. Simeoni, S. Mengali, M. Zalkovskij, B. Bilenberg, C. De Groot, and O. L. Muskens, "Metasurface optical solar reflectors using AZO transparent conducting oxides for radiative cooling of spacecraft," ACS Photonics **5**(2), 495–501 (2018).
11. Y. Zhai, Y. Ma, S. N. David, D. Zhao, R. Lou, G. Tan, R. Yang, and X. Yin, "Scalable-manufactured randomized glass-polymer hybrid metamaterial for daytime radiative cooling," Science **355**(6329), 1062–1066 (2017).
12. X. Shi, Z. Qin, Z. Liang, D. Meng, J. Li, S. Zhang, R. Dai, E. Hou, W. Xin, H. Liu, H. Xu, and Y. Liu, "Polarization-selective absorptive and transmissive metamaterials," Opt. Express **30**(12), 20532–20542 (2022).
13. D. Hasan and C. Lee, "Hybrid Metamaterial Absorber Platform for Sensing of CO2 Gas at Mid-IR," Adv. Sci. **5**(5), 1700581 (2018).
14. J. Y. Suen, K. Fan, J. Montoya, C. Bingham, V. Stenger, S. Sriram, and W. J. Padilla, "Multifunctional metamaterial pyroelectric infrared detectors," Optica **4**(2), 276–279 (2017).
15. J. Kim, C. Park, and J. W. Hahn, "Metal–Semiconductor–Metal Metasurface for Multiband Infrared Stealth Technology Using Camouflage Color Pattern in Visible Range," Adv. Opt. Mater. **10**(6), 2101930 (2022).
16. T. Kim, J. Y. Bae, N. Lee, and H. H. Cho, "Hierarchical metamaterials for multispectral camouflage of infrared and microwaves," Adv. Funct. Mater. **29**(10), 1807319 (2019).
17. Z. Liao, Z. Liu, Y. Wang, X. Liu, and G. Liu, "Ultra-narrowband resonant light absorber for high-performance thermal-optical modulators," Opt. Express **29**(20), 31048–31057 (2021).
18. J. Jung, J. Lee, J. Choi, D. Choi, and J. Jeong, "Enhancement of refractive index sensing for an infrared plasmonic metamaterial absorber with a nanogap," Opt. Express **29**(14), 22796–22804 (2021).
19. C. Guo, Y. Guo, B. Lou, and S. Fan, "Wide wavelength-tunable narrow-band thermal radiation from moiré patterns," Appl. Phys. Lett. **118**(13), 131111 (2021).
20. K. Sun, Z. Zhao, Y. Cai, U. Levy, and Z. Han, "Ultra-narrowband and highly-directional THz thermal emitters based on the bound state in the continuum," Nanophotonics **10**(16), 4035–4043 (2021).
21. D. D. Kang, T. Inoue, T. Asano, and S. Noda, "Demonstration of a mid-wavelength infrared narrowband thermal emitter based on GaN/AlGaN quantum wells and a photonic crystal," Appl. Phys. Lett. **110**(18), 181109 (2017).
22. S. Kang, Z. Qian, V. Rajaram, S. D. Calisgan, A. Alù, and M. Rinaldi, "Ultra-narrowband metamaterial absorbers for high spectral resolution infrared spectroscopy," Adv. Opt. Mater. **7**(2), 1801236 (2019).
23. L. Meng, D. Zhao, Z. Ruan, Q. Li, Y. Yang, and M. Qiu, "Optimized grating as an ultra-narrow band absorber or plasmonic sensor," Opt. Lett. **39**(5), 1137–1140 (2014).
24. B. Wang, W. Huang, and L. Wang, "Ultra-narrow terahertz perfect light absorber based on surface lattice resonance of a sandwich resonator for sensing applications," RSC Adv. **7**(68), 42956–42963 (2017).
25. Z. Li, X. Sun, C. Ma, J. Li, X. Li, B. Guan, and K. Chen, "Ultra-narrow-band metamaterial perfect absorber based on surface lattice resonance in a WS2 nanodisk array," Opt. Express **29**(17), 27084–27091 (2021).
26. L. Meng, D. Zhao, Y. Yang, F. J. G. De Abajo, Q. Li, Z. Ruan, and M. Qiu, "Gain-assisted plasmon resonance narrowing and its application in sensing," Phys. Rev. Applied **11**(4), 044030 (2019).
27. K. Koshelev, S. Kruk, E. Melik-Gaykazyan, J. Choi, A. Bogdanov, H. Park, and Y. Kivshar, "Subwavelength dielectric resonators for nonlinear nanophotonics," Science **367**(6475), 288–292 (2020).
28. E. Tiguntseva, K. Koshelev, A. Furasova, P. Tonkaev, V. Mikhailovskii, E. V. Ushakova, D. G. Baranov, T. Shegai, A. A. Zakhidov, and Y. Kivshar, "Room-temperature lasing from Mie-resonant nonplasmonic nanoparticles," ACS Nano **14**(7), 8149–8156 (2020).
29. M. L. Tseng, M. Semmlinger, M. Zhang, C. Arndt, T. Huang, J. Yang, H. Y. Kuo, V. Su, M. K. Chen, and Chu C. H. J. S. a, "Vacuum ultraviolet nonlinear metalens," Sci. Adv. **8**(16), eabn5644 (2022).
30. Z. Xuan, J. Li, Q. Liu, F. Yi, S. Wang, and W. Lu, "Artificial Structural Colors and Applications," Innovation **2**(1), 100081 (2021).
31. F. Balli, M. A. Sultan, A. Ozdemir, and J. T. Hastings, "An ultrabroadband 3D achromatic metalens," Nanophotonics **10**(4), 1259–1264 (2021).
32. M. Pan, Y. Fu, M. Zheng, H. Chen, Y. Zang, H. Duan, Q. Li, M. Qiu, and Y. Hu, "Dielectric metalens for miniaturized imaging systems: progress and challenges," Light: Sci. Appl. **11**(1), 195 (2022).
33. A. Majumdar and S. Colburn, "Polarization-controlled optical holography using flat optics," Light: Sci. Appl. **9**(1), 134 (2020).
34. P. Georgi, Q. Wei, B. Sain, C. Schlickriede, Y. Wang, L. Huang, and T. Zentgraf, "Optical secret sharing with cascaded metasurface holography," Sci. Adv. **7**(16), eabf9718 (2021).

35. A. I. Kuznetsov, A. E. Miroshnichenko, M. L. Brongersma, Y. S. Kivshar, and B. Luk'yanchuk, "Optically resonant dielectric nanostructures," Science **354**(6314), aag2472 (2016).

36. S. J. Kim, J. Park, M. Esfandyarpour, E. F. Pecora, P. G. Kik, and M. L. Brongersma, "Superabsorbing, Artificial Metal Films Constructed from Semiconductor Nanoantennas," Nano Lett. **16**(6), 3801–3808 (2016).

37. S. Tretyakov, "Maximizing absorption and scattering by dipole particles," Plasmonics **9**(4), 935–944 (2014).

38. X. Ming, X. Liu, L. Sun, and W. J. Padilla, "Degenerate critical coupling in all-dielectric metasurface absorbers," Opt. Express **25**(20), 24658–24669 (2017).

39. R. Xu and J. Takahara, "All-dielectric perfect absorber based on quadrupole modes," Opt. Lett. **46**(15), 3596–3599 (2021).

40. J. Tian, Q. Li, P. A. Belov, R. K. Sinha, W. Qian, and M. Qiu, "High-Q all-dielectric metasurface: super and suppressed optical absorption," ACS Photonics **7**(6), 1436–1443 (2020).

41. J. Yu, B. Ma, A. Ouyang, P. Ghosh, H. Luo, A. Pattanayak, S. Kaur, M. Qiu, P. Belov, and Q. Li, "Dielectric super-absorbing metasurfaces via PT symmetry breaking," Optica **8**(10), 1290–1295 (2021).

42. J. Tian, H. Luo, Q. Li, X. Pei, K. Du, and M. Qiu, "Near-infrared super-absorbing all-dielectric metasurface based on single-layer germanium nanostructures," Laser Photonics Rev. **12**(9), 1800076 (2018).

43. C. Yang, J. Yang, Z. Yang, Z. Zhou, M. Sun, V. E. Babicheva, and K. Chen, "Nonradiating silicon nanoantenna metasurfaces as narrowband absorbers," ACS Photonics **5**(7), 2596–2601 (2018).

44. L. Liu, L. Kang, T. S. Mayer, and D. H. Werner, "Hybrid metamaterials for electrically triggered multifunctional control," Nat. Commun. **7**(1), 13236 (2016).

45. R. Xu, J. Luo, J. Sha, J. Zhong, Z. Xu, Y. Tong, and Y.-S. Lin, "Stretchable IR metamaterial with ultra-narrowband perfect absorption," Appl. Phys. Lett. **113**(10), 101907 (2018).

46. S. Yu, Z. Li, W. Liu, H. Cheng, Y. Zhang, B. Xie, W. Zhou, J. Tian, and S. Chen, "Tunable dual-band and high-quality-factor perfect absorption based on VO2-assisted metasurfaces," Opt. Express **29**(20), 31488–31498 (2021).

47. M. Pan, H. Huang, W. Chen, S. Li, Q. Xie, F. Xu, D. Wei, J. Fang, B. Fan, and L. Cai, "Design of Narrow-Band Absorber Based on Symmetric Silicon Grating and Research on Its Sensing Performance," Coatings **11**(5), 553 (2021).

48. N. Wada, S. Solin, J. Wong, and S. Prochazka, "Raman and IR absorption spectroscopic studies on α, β, and amorphous Si3N4," J. Non-Cryst. Solids **43**(1), 7–15 (1981).

49. C. Ma, J. Yan, Y. Huang, C. Wang, and G. Yang, "The optical duality of tellurium nanoparticles for broadband solar energy harvesting and efficient photothermal conversion," Sci. Adv. **4**(8), eaas9894 (2018).